CrossMark

ORIGINAL ARTICLE

Mohammad Reza Salimi · Mohammad Taeibi Rahni ·
Freydun Jam

Pore-scale simulation of fluid flow passing over a porously covered square cylinder located at the middle of a channel, using a hybrid MRT-LBM–FVM approach

Abstract A comprehensive study was performed to analyze the unsteady laminar flow characteristics around a porously covered, a fully porous, and a solid squared section cylinder located in the middle of a plane channel. In order to simulate fluid flow inside porous media and porous–fluid interface accurately (minimizing modeling error), the porous region was analyzed in pore scale, using LBM. Additionally, to minimize the LBM-related compressibility error through the porous region, a multi-block multiple relaxation time lattice Boltzmann method (MRT-LBM) was used. Also, to decrease CPU time, a Navier–Stokes flow solver, based on finite volume method and SIMPLE algorithm, was coupled with MRT-LBM to simulate flow around the porous obstacle. It should be noted that the flow inside the porous layer is in continuum regime, and hence, the no-slip boundary condition was used to treat the solid walls inside the porous media. In our simulations, we considered variations of porosity and Reynolds number ranging from 0.75 to 0.94 and from 60 to 240, respectively. The effects of porosity and Reynolds number on vortex pattern, mean drag coefficient, amplitude of lift coefficient, and Strouhal number were investigated. Comparison of our results with the ones obtained using Open FOAM, as well as published by others, shows the suitable accuracy of our computations. It is seen that at low Reynolds numbers or at low porosities, where the mean flow does not have large enough momentum to penetrate porous media, the resulting flow field and aerodynamic coefficients are relatively close for three different configurations used. However, as the flow Reynolds number or permeability increases, the mean flow penetrates easier into the porous media and thus provides different shedding characteristics and aerodynamic coefficients for different obstacle shapes.

Keywords Hybrid LBM–FVM · Porous media · Pore-scale simulation · Unsteady flow

1 Introduction

Flow and heat transfer in porous media are important in many scientific and engineering fields. On the other hand, flow through a porous medium in a channel has various practical applications, such as LED backlight module cooling systems, drying processes, heat exchangers, heat pipes, and cooling of electronic equipment. As another important example, porous media are used to reduce vortex- induced vibrations (VIV) in many engineering applications [1–4]. This is because, vortex shedding frequency can be close to a structural resonant

M. R. Salimi · M. Taeibi Rahni (✉)
Aerospace Engineering Department, Sharif University of Technology, Tehran, Iran
E-mail: taeibi@sharif.edu

F. Jam
Mechanical Engineering, Farab Co., Tehran, Iran

frequency or can make electromagnetic noise in electronic devices [1]. Hence, in the past two decades, numerous investigations have been conducted to characterize the flow and heat transfer through porous materials (especially, porous blocks and porous layers).

Huang and Vafai [5] performed a fundamental investigation on the effects of using alternately placed porous cavity-block wafers to control skin friction and heat transfer characteristics of an external surface and found that this configuration has noticeable effects. Jue [6] explored unsteady vortex shedding behind a porous squared section cylinder in which the effects of permeability, porosity, and Reynolds number on lift and drag coefficients and also on Strouhal number were studied. According to their results, permeability and Reynolds number have significant influences on vortex structure and shedding period. Likewise, Chen et al. [7] performed a numerical simulation of flow past a porous squared section cylinder, considering stress jump treatment for the porous–fluid interface. Their simulations were presented for various Reynolds numbers (20–250), Darcy numbers (10–2–10–5), and porosity (0.4–0.8). Their results indicated that stress jump interface condition can result in flow instability and changes in vortex structures. Bruneau and Mortazavi [8] showed that wrapping a porous layer around a squared cylinder is able to reduce vortex-induced vibration and drag coefficient noticeably. Similarly, Rong et al. [9] conducted a numerical study, using LBM, to investigate flow around a porously covered solid cylinder. They employed Darcy–Brinkman–Forchheimer equation to model the flow inside porous medium. Their results indicated that both drag and lift coefficient amplitudes increase, as the porous layer thickness increases. Moreover, they found that among considered parameters, effect of porosity is negligible, whereas the influence of Darcy number (Da) is dominant.

Wu and Wang [10] analyzed unsteady flow and heat transfer across a porous squared cylinder located at the middle of a channel. They investigated the effects of parameters including Reynolds number, Darcy number, and porosity. Later, Perng et al. [11] extended their previous work by considering the effects of cylinder-to-channel width ratio along with the aforementioned parameters. Liang et al. [12] also conducted a numerical analysis to look into the effects of mean flow pulsation on flow and heat transfer characteristics of a porous block-mounted heat source located at the middle of a channel. Their results showed that the periodic alteration of the recirculation zone in the vicinity of the porous block has a direct impact on heat transfer rate.

In the above cited works, the volume-averaged approaches (Brinkman–Forchheimer-extended Darcy model) were extensively used to characterize the flow and heat transfer inside the porous region. However, for complex porous structures with spatially non-uniform porosity or highly tortuous fluid passages [13], the pore-scale modeling leads to much more accurate prediction of macroscopic properties in porous media. Particularly, when a fluid flows through porous media at high Peclet numbers, one should take into account the effects of dispersion, which is resolved accurately using pore-scale modeling [14]. Moreover, the proper implementation of the porous-plane interface boundary condition, as shown by Chen et al. [7], can affect the flow structures in certain problems, while the porous-plane interface is automatically modeled when using pore-scale modeling.

In recent years, LBM has been successfully applied to simulate transport phenomena in complex geometries, such as porous media. Consequently, there are many investigations in literature characterizing flow, heat, and mass transfer at pore level in porous structures, using LBM. For example, Cancelliere et al. [13] computed permeability for a three-dimensional porous structure constructed from randomly distributed solid particles. On the other hand, Inamuro et al. [14,15] analyzed flow, heat, and mass transfer through an infinite number of spheres in different Reynolds numbers. On the other hand, Wang et al. [16] used LBM to determine effective thermal conductivity in fibrous porous materials. In addition, in recent years, numerous investigations have been performed in different engineering applications, considering heat and mass transfer in porous structures (in pore scale), using LBM [17–19].

Many problems in science and engineering, including material science, mechanics, and electronics have multi-scale nature [1]. Also, the study of transport phenomena through porous blocks in a channel is a macro-/mesoscale problem. For such problems, using a single macro-level numerical approach (such as classical CFD) and Brinkman–Forchheimer-extended Darcy model leads to loss of considerable amount of details related to local mesoscale transports. On the other hand, using a single mesoscale method to analyze the entire domain is computationally inefficient. Therefore, for such problems, different numerical approaches must be applied to simulate the processes at different length and timescales. In a multi-scale problem, generally, the computational domain is decomposed into two or more sub-domains and different computational approaches are implemented. In view of high computational benefits, the coupling between various classical CFD methods, including FDM [20,21] and FVM [22–25], with LBM have been the subject of wide interests in recent years.

This work aims at characterizing unsteady laminar flow around a porously covered solid block, and the results were compared with those of solid and fully porous squared blocks. Simulations were performed in three

different porosity of 0.75, 0.85, and 0.94 and also at seven different Reynolds numbers of 60, 120, 140,160, 180, 200, and 240.

Multiple relaxation time lattice Boltzmann method (MRT-LBM) is utilized to simulate flow through the porous media (in pore level) owing to its strength in handling fluid flow in geometrically complex boundaries, whereas the FVM (based on NS equations) is implemented to simulate the external flow field around the porous block (because of its capabilities to reduce the computational cost, using stretched computational grid). The MRT-LBM is used due to its superior capabilities over the SRT-LBM version. For instance, since in MRT, different modes use different relaxation times and bulk and shear viscosities can be adjusted independently. Hence, large bulk viscosity can be used along with very low shear viscosity. Large bulk viscosity helps to damp spurious pressure waves generated due to poor initial conditions or geometric singularities [28]. Thus, using MRT-LBM model can effectively increase numerical stability and accuracy (in unsteady flows). Moreover, in SRT model, the location of solid wall depends on viscosity, which pose a severe problem for simulating flow in porous media (since permeability becomes viscosity dependent, it should be a characteristic of physical properties of the porous medium alone) [29]. However, MRT model can effectively reduce the viscosity-dependent permeability problem and hence increases the simulation accuracy inside porous regions [29].

The innovative aspects of the present study are as follows:

1. analyzing unsteady vortex shedding of a porously covered, fully porous, and solid squared cylinder confined in a channel,
2. simulation of fluid flow through and around porous obstacles in pore level, and
3. using MRT-LBM, along with a Navier–Stokes-based finite volume method (SIMPLE algorithm), as a hybrid FV-LB (MRT) method to simulate unsteady fluid flow around porous obstacles.

2 Statement of the problem

In this work, fluid flow around a solid (Fig. 1a), a porously covered (Fig. 1b), and a fully porous (Fig. 1c) two-dimensional squared section cylinder with height (D) mounted in the middle of a plane channel was investigated (Fig. 1). The flow was assumed laminar, incompressible, and unsteady (constant molecular properties of both fluid and the porous media). The velocity profile at the entrance of the channel was assumed to be parabolic with maximum velocity u_0. The ratio L/D (channel length/porous block widths) was set to 31, and the blockage ratio (porous block width/channel width) was $\beta = D/H = 1/4$. For porously covered cylinder (Fig. 1b), the thickness of the porous layer (h) was $0.18D$ and the central solid block width (d) was $0.64D$. The porous media was constructed using a collection of solid squared particles arranged in a homogenous manner (except close to the solid boundaries). It should be noted that, in this work, the flow field inside porous media is still in continuum regime and no-slip boundary condition is used to treat solid boundaries. Three different porosities (ε) of 0.75, 0.85, and 0.94 (conventional porosity for metal foams [26,27]) were produced by varying the
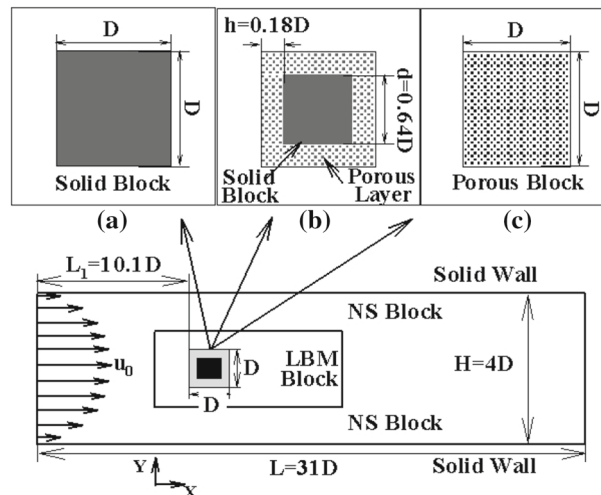

Fig. 1 Schematic of the problem under consideration. **a** solid block, **b** solid block covered with a porous layer, **c** porous block

Fig. 2 Schematic of the generated grid and blocks arrangement in LB and N–S computational domains

spatial density of solid particles. The corresponding permeability (K) was computed for each porosity, using a pore-scale modeling of a fully filled channel (explained in subsequent sections). For porosities of 0.75, 0.85, and 0.94, the related permeability was computed to be 1.602, 4.811, and 41.83 (Lu^2), respectively (Lu^2 is the lattice unit length squared). Besides, based on the obstacle height (D), the mentioned permeabilities correspond to Darcy numbers of 2.06×10^{-4}, 6.21×10^{-4}, and 5.4×10^{-3}, respectively.

Simulations were performed in seven different inflow Reynolds numbers (based on porous block height D and maximum inlet velocity u_0) of 60, 120, 140, 160, 180, 200, and 240. The computational domain was divided into two sub-domains, the outer (larger) sub-domain being analyzed by a conventional CFD (FVM) approach, while the inner (smaller) sub-domain was analyzed by LBM.

The computational grid in FVM subregion was non-uniform and was refined toward the LBM subregion (from all directions) to reduce computational cost. Also, most computational cells were concentrated about the central LBM region through grid refining, in which the flow physics was more complicated. In the LBM sub-domain, the computational mesh (Fig. 2) was refined in two steps (by a factor of 2 in each step). Finally, at the NS–LB and LB–LB block interfaces, four computational nodes from finer block were overlapped with the corresponding grid points from coarser block to assure a smooth flow field.

3 Numerical formulation and boundary conditions

As shown in Fig. 1, the computational domain is divided into three different regions: a FVM region where NS equations are solved, a LBM region where lattice Boltzmann equation is solved, and an interface between the two where the resulting information is exchanged. In this section, the governing equations for FVM, LBM, and interface sub-domains are discussed. Additionally, the boundary conditions implemented are explained.

3.1 Navier–Stokes equations

The conservative form of the NS equations for two-dimensional incompressible flows without body forces can be written in Cartesian coordinate system, as:

Continuity equation:

$$\frac{\partial (\rho u_i)}{\partial x_i} = 0, \tag{1}$$

Momentum equation:

$$\frac{\partial (\rho u_i)}{\partial t} + \frac{\partial (\rho u_i u_j)}{\partial x_j} = -\frac{\partial p}{\partial x_i} + \mu \left(\frac{\partial^2 u_i}{\partial x_j \partial x_j} \right). \tag{2}$$

In order to solve these equations, finite volume method and unsteady SIMPLE algorithm on a collocated grid were used to provide a coupling between pressure and velocity fields. For spatial discretization of flux vector, QUICK algorithm was used along with Crank–Nicholson scheme for time integration. Hence, the provided Navier–Stokes solver is second order accurate in both time and space.

3.2 Lattice Boltzmann method

The most popular kinetic model adopted widely in literature is the single relaxation time (SRT) approximation and the so-called Bhatnagar–Gross–Krook (BGK) model, namely:

$$\frac{\partial f}{\partial t} + c \cdot \nabla f = -\frac{1}{\lambda}\left(f - f^{(eq)}\right), \tag{3}$$

where f denotes a single particle distribution function, $f^{(eq)}$ is equilibrium distribution function, λ is relaxation time, and c is particle velocity vector. Since collision operator in SRT model is approximated by single relaxation time, it usually has numerical instability (at very low relaxation times) and viscosity dependence of boundary location problems. The viscosity dependence of the solid boundary location can produce severe problems for simulating flow in porous materials [28,29]. The viscosity-dependent boundary location problem in the SRT model can be removed by using sufficiently fine grid in pore volumes. However, applying such a fine grid is computationally very expensive, especially in three-dimensional simulations. This inherent deficiency of SRT model can be adequately improved using MRT model [29], such that much less grid resolution is needed to achieve the same accurately. Here, D2Q9-MRT-LBM with the following time evolution equation was used:

$$f_i\left(x + e_i\delta t, t_n + \delta t\right) - f_i\left(x, t_n\right) = -M^{-1}S\left[m_i\left(x, t_n\right) - m_i^{eq}\left(x, t_n\right)\right], \tag{4}$$

where $m_i\left(x, t_n\right)$ and $m_i^{eq}\left(x, t_n\right)$ are the nine components of linear moment vector and their corresponding equilibrium. The relaxation matrix (S) is a nonnegative diagonal matrix consisting of nine relaxation rates, s_α. The transformation matrix (M) is orthogonal and maps $f_i\left(x, t_n\right)$ vector to $m_i\left(x, t_n\right)$ vector. In addition, for D2Q9 model, the discrete velocities (e_i) are as follows:

$$e_i = \begin{cases} (0, 0), & i = 0, \\ (\pm c, 0), (0, \pm c), & i = 1, 2, 3, 4, \\ (\pm c, \pm c). & i = 5, 6, 7, 8, \end{cases} \tag{5}$$

where $c = \delta x/\delta t$, $\delta x = 1$, and $\delta t = 1$ are the lattice length and time steps, respectively. Also the nine macroscopic moments are as follows:

$$m = \left(\rho, e, \varepsilon, j_x, q_x, j_y, q_y, p_{xx}, p_{xy}\right)^T. \tag{6}$$

These nine moments have the following physical meanings: ρ is fluid density, e, and ε are related to the energy and energy squared, respectively, j_x and j_y are momentum components, q_x and q_y are related to components of energy fluxes, and p_{xx} and p_{xy} correspond to the diagonal and off-diagonal components of viscous stress tensor, respectively. The equilibrium moments (m^{eq}) can be constructed as:

$$\begin{aligned} &m_0^{eq} = \rho, \quad m_3^{eq} = \rho u, \quad m_5^{eq} = \rho v, \\ &m_1^{eq} = -2\rho + 3\left(j_x^2 + j_y^2\right)/\rho, \quad m_2^{eq} = \rho - 3\left(j_x^2 + j_y^2\right)/\rho, \quad m_4^{eq} = -j_x, \\ &m_6^{eq} = -j_y, \quad m_7^{eq} = \left(j_x^2 - j_y^2\right)/\rho, \quad m_8^{eq} = \left(j_x j_y\right)/\rho, \end{aligned} \tag{7}$$

in which fluid density (ρ) and momentum flux (ρu) are given as:

$$\rho = \sum_i f_i, \quad \rho \boldsymbol{u} = \left(j_x, j_y\right) = \sum_i e_i f_i, \tag{8}$$

The transport matrix (M) can be written as [29]:

$$
M = \begin{bmatrix}
1 & 1 & 1 & 1 & 1 & 1 & 1 & 1 & 1 \\
-4 & -1 & -1 & -1 & -1 & 2 & 2 & 2 & 2 \\
4 & -2 & -2 & -2 & -2 & 1 & 1 & 1 & 1 \\
0 & 1 & 0 & -1 & 0 & 1 & -1 & -1 & 1 \\
0 & -2 & 0 & 2 & 0 & 1 & -1 & -1 & 1 \\
0 & 0 & 1 & 0 & -1 & 1 & 1 & -1 & -1 \\
0 & 0 & 2 & 0 & 2 & 1 & 1 & -1 & -1 \\
0 & 1 & -1 & 1 & -1 & 0 & 0 & 0 & 0 \\
0 & 0 & 0 & 0 & 0 & 1 & -1 & 1 & -1
\end{bmatrix}
\tag{9}
$$

While the relaxation diagonal matrix (S) is:

$$
S = [s_0, s_1, s_2, s_3, s_4, s_5, s_6, s_7, s_8],
\tag{10a}
$$

in which the collision rates s_0, s_3, and s_5 are related to the conserved moments and can take the value of 0 to enforce mass and linear momentum conservations [29]. In order to reproduce the same viscosity as that of SRT model, s_7 and s_8 must be set to $\frac{1}{\lambda}$. The other relaxation rates have no physical meaning for incompressible flows and can be chosen in the range: $0 < s_i < 2$. In the present work, the following relaxation parameters were used [29]:

$$
s_1, s_2, s_3, s_5, s_7, s_8 = \frac{1}{\tau} \qquad s_4, s_6 = 8\frac{2 - \frac{1}{\tau}}{8 - \frac{1}{\tau}}
\tag{10b}
$$

As shown in Fig. 2, in order to offer a higher grid resolution near obstacles, multi-block method for the MRT scheme (derived by Peng et al. [30]) was implemented.

3.3 Interface treatment

To construct a hybrid LB–NS method, the main task is transformation of flow variables from macroscales (Navier–Stokes) to mesoscales (Lattice Boltzmann) and vice versa. To transform the mesoscale parameters into macroscale ones, some compression or restriction operator is needed [30]. It should be noted that, in the present paper, the mesoscale is used to refer to the LBM length and timescales. Thus, the mesoscale does not means non-continuum or even a continuum with slip wall boundary condition flow here. For LBM, the compression operators are presented in Eq. (8), and thus, computing macroscopic variables from distribution functions is straightforward. In addition to Eq. (8), to compute pressure (for the pressure-based SIMPLE algorithm), the following relation was used:

$$
P_{NS} = P_{NS}^0 + (\rho_{LB} - \rho_0) c_s^2,
\tag{11}
$$

in which P_{NS}^0 is the base pressure in NS domain which is set to zero here, while ρ_0 is the initial density, which has the same value for both LBM and FVM solvers. In contrast, while using restriction step, there exist no one-to-one mapping between macroscopic variables and particle distribution functions in the lifting or reconstruction step. In this work, the reconstruction operator proposed by Xu et al. [31] was implemented to compute the mesovariables (f) from macrovariables (ρ and u) as follows:

$$
f_i = f_i^{(eq)} \left[1 - \frac{\lambda \Delta t U_{i\beta}}{c_s^2} \left(U_{i\alpha} \partial_{x_\alpha} u_\beta + \upsilon \partial_{x_\alpha}^2 u_\beta + \frac{\upsilon}{\rho} S_{\alpha\beta} \partial_{x_\alpha} \rho \right) \right].
\tag{12}
$$

This relation approximates a single particle distribution function f_i up to second power of ε. Note, in Eq. (12), υ is kinematic viscosity and $S_{\alpha\beta}$ is strain rate. Also, peculiar velocity ($U_{i\alpha}$) is computed as follows:

$$
U_{i\alpha} = C_{i\alpha} - U_\alpha.
\tag{13}
$$

3.4 Boundary conditions

At the inlet of the Navier–Stokes sub-domain, a parabolic profile was used for streamwise velocity component, while the y-component of velocity was set to zero. At its outflow, however, the gradient of y-velocity component was set to zero. Also, to ensure conservation of mass, the following relation for the streamwise velocity was applied:

$$U_{NI} = (\dot{m}_{in}/\dot{m}_{out})\, U_{NI-1}, \tag{14}$$

where $\dot{m}_{in}$ and $\dot{m}_{out}$ are total inlet and outlet mass flow rates, respectively. Based on Eq. 14, the streamwise velocity component of the last computational cell in x-direction (U_{NI}) is set to its previous cell value (U_{NI-1}) times a mass flow correction factor ($\dot{m}_{in}/\dot{m}_{out}$). Hence, the axial velocity in the last computational cell is tuned in such way to ensure mass conservation throughout the computational domain (to increases the numerical stability). When inlet and outlet mass flow rates became equal, this boundary condition reduces to a simple zero gradient condition on the axial velocity component. Also, for upper and lower solid walls, no-slip boundary condition was used. In lattice Boltzmann sub-domain, the midpoint bounce back boundary condition was applied at the solid boundaries. At the interface region, the post-collision distribution functions were computed using Eq. (12).

4 Validations and verifications

Two classic problems were used to verify the present hybrid FVM–LBM (MRT) solver: (1) a porous channel being fully filled with porous material (Fig. 3), analyzed in pore scale to evaluate LBM-MRT solver and (2) flow field around a solid squared cross-sectional cylinder (for validation of hybrid NS–LBM code).

4.1 Fully filled channel flow

Flow through a parallel channel, filled with uniformly distributed solid squared obstacles (Fig. 3) was simulated, using LBM (MRT) with two different porosities (0.75 and 0.85). The same pore structures were used in all porous media of this work (porous covers and blocks).

Note, for grid independency study, five different grids 4×4, 6×6, 8×8, 10×10, and 16×16 were used to resolve each obstacle. The resulting permeabilities were evaluated for these five grids and were summarized (Table 1). The pressure difference (Δp) between inlet and outlet and the resulting mass flow rate ($\dot{m}$) were
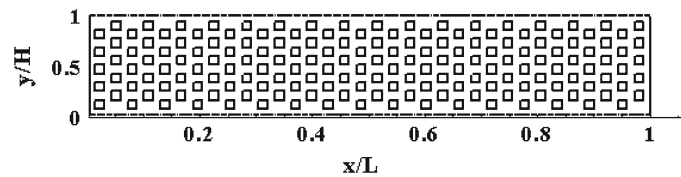

Fig. 3 Schematic of the pore structures in fully filled plane channel at $\varepsilon = 0.75$

Table 1 Grid dependency study using permeability for different obstacle sizes ($\varepsilon = 0.75$ and $\varepsilon = 0.85$)

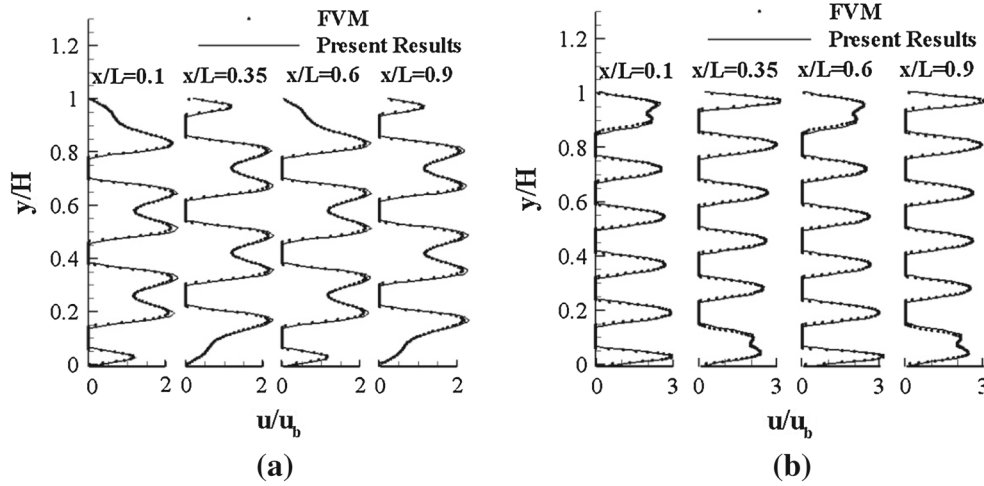| Obstacle size	Permeability (Lu^2)	FVM permeability (10×10 obstacle size) (Lu^2)
$\varepsilon = 0.75$		
4×4	1.891	1.575
6×6	1.633	
8×8	1.595	
10×10	1.572	
16×16	1.568	
$\varepsilon = 0.85$		
4×4	4.477	4.901
6×6	4.720	
8×8	4.811	
10×10	4.853	
16×16	4.880	

Fig. 4 Non-dimensional streamwise velocity profiles in various x locations for **a** $\varepsilon = 0.75$ and **b** $\varepsilon = 0.85$

used to compute permeability in Darcy regime. In each case, Δp was adjusted in such a way to produce two Reynolds numbers: one in the range $0.1 < Re_p < 0.4$ and the other in the range $0.7 < Re_p < 1.0$ (Re_p is based on the particles width and averaged velocity). The permeability was then computed as $K = \frac{\upsilon \dot{m}}{H \nabla P}$ (H is the channel width and υ is the kinematic viscosity) for each pressure gradient. In all cases in Table 1, the difference between these two permeability is negligible, which indicates that the resulting permeability is independent of Re_p (In Darcy regime $Re_p < 1$). As presented in Table. 1, for $\varepsilon = 0.75$, the difference between the result of the fifth grid (16×16) with second, third, and fourth grids is 4.1, 1.7, and 0.2 %, respectively. Similarly, for $\varepsilon = 0.85$, the computed error for second, third, and fourth grids compared to the fifth one is 3.3, 1.4, and 0.5 %, respectively. Additionally, the resulting permeability of FVM on 10×10 grid is also presented for comparison. As shown in Table 1, there are good agreements between the results of LBM and FVM. Based on these comparisons, the third grid was used for all simulations.

In Fig. 4, the non-dimensioned streamwise velocity component (u/u_b) prediction of LBM and that of the well-known Open FOAM solver are compared in streamwise locations $x/L = 0.1, 0.35, 0.6,$ and 0.9 when the pressure difference between the inlet and outlet was 0.003. This pressure gradient corresponds to $Re_p = 8.3$ for $\varepsilon = 0.75$ and $Re_p = 14.8$ for $\varepsilon = 0.85$. The flow was steady in both cases and the bulk axial velocity (u_b) was computed using the relation: $u_b = \frac{1}{H} \int_0^H u \mathrm{d}y$. The channel height ($H$), channel length ($L$), and particles height (D) were 70, 383, and 8 (in lattice unit), respectively. Also, the relaxation time (τ) was 0.505 (corresponding to $\nu = 1.6835 \times 10^{-3}$). The following set up was also used in Open FOAM CFD code. The incompressible Navier–Stokes equations were discretized using FVM and pressure-based SIMPLE algorithm. Moreover, the momentum equation was discretized using a second-order upwind scheme on a uniform Cartesian (squared shape) grid. As illustrated in Fig. 4, there are close agreements between LBM and Open FOAM results (in both porosities of 0.75 and 0.85).

4.2 Confined flow around a squared section cylinder

In order to make a detailed validation of our hybrid FVM–LBM (MRT) flow solver, confined flow past a squared section cylinder, mounted at the middle of a plane channel, was simulated for $Re = 100$ (based on squared cylinder height and maximum inflow velocity) and for blockage ratio (cylinder-to-channel width ratio) of 0.125. The block located at $L = 12.5D$ from the entrance of the channel, and the channel length was set to $45D$. In addition, a parabolic x-velocity profile with maximum streamwise velocity of u_{Max} was used at the entrance of the channel. The streamwise and the lateral non-dimensioned velocity profiles, $u(y)/u_{\mathrm{Max}}$ and $v(y)/u_{\mathrm{Max}}$ at $x/D = 0$ (cylinder centerline), are compared to the numerical results of Breuer et al. [32] in Fig. 5a, while in Fig. 5b, similar comparison is made between streamwise velocity components $u(x)/u_{\mathrm{Max}}$ at $y/D = 0$. Since flow is unsteady at this Re, the time level, at which the lateral velocity component $v(y)/u_{\mathrm{Max}}$ crosses 0 (from minus to plus) at an axial position of $10D$ downstream of the cylinder, was selected to evaluate the instantaneous velocity profiles. It is clear from Fig. 5 that the discrepancies between the hybrid method
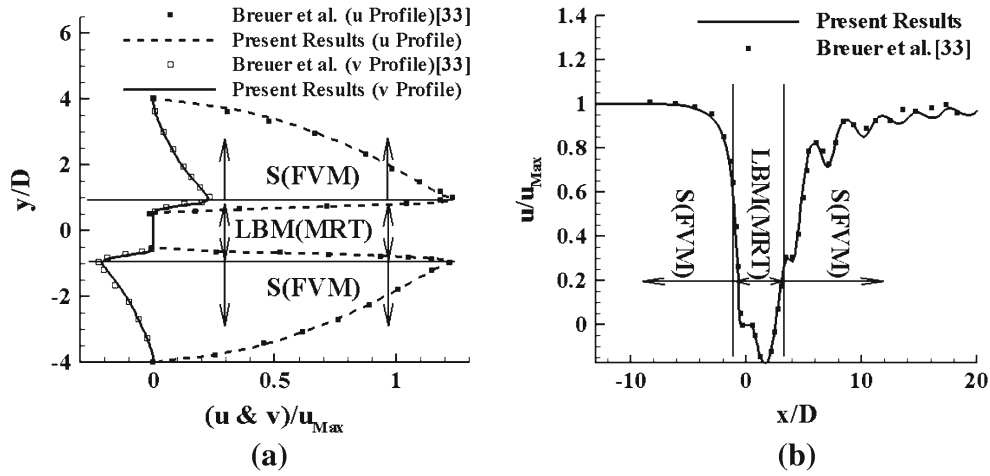
Fig. 5 Comparison between velocity profiles of present simulations and those of Breuer et al. [32]: **a** streamwise and lateral components at $x/D = 0$ and **b** streamwise velocity component at $y/D = 0$

profiles and those of Breuer et al. [32] are small. Additionally, the smoothness of these plots (especially around the interface region) gives a clear picture of the accuracy of the information exchanged between FVM and LBM solvers.

As a result, it is observed that the present hybrid FVM–LBM (MRT) flow solver is capable of predicting unsteady separated flow around bluff bodies (i.e. porous blokes) accurately with much lower computational cost (comparing to fully LBM simulation). This is first due to using a NS-based solver for non-porous region needing much fewer grid points (because of the capability of employing a non-uniform mesh). Second, the SIMPLE algorithm has an implicit nature, giving the ability of using larger time steps and consequently less iterations for unsteady calculations.

5 Computational benefits of hybrid method

By definition, in a multi-scale problem, different physical phenomena occur in considerably different length and timescales [24,25]. For instance, there are several problems in science and engineering dealing with either macro-/microscale or macro-/mesoscale phenomena. In CFD, different computational methods have been developed to simulate such problems accurately [24,25,35]. For example, MD is the most accurate method for nanoscale problems, LBM for mesoscale ones, and NS-based methods for macroscale ones. Using incorrect numerical method (regarding the length and timescales) violates the numerical accuracy or reduces computational efficiency. Thus, in order to achieve the most accurate results with minimum computational cost for multi-scale problems, the hybrid numerical methods (such as NS–LB, NS–MD, and LB–MD) have been developed in recent years [35].

In the present work, the interaction between fluid flow and porous obstacles (the porous media is threaded in pore scale) is simulated as a macro-/mesoscale problem. LBM (first order accurate in time and second order in space) is used to treat flow in porous region, while NS-based FVM (which is second order in both time and space here) is used to simulate the rest of the flow. LBM is employed due to its superior capability in handling complex geometries accurately, while FVM is used to increase computational efficiency. Thus, the main goal of using hybrid FVM–LBM in the present research is to increase computational accuracy in porous region with the aid of LBM. Moreover, in this section, it is illustrated that the numerical efficiency of the hybrid method used is also higher than both pure LBM and pure FVM (with the same grid resolution and hence numerical accuracy) to handle the multi-scale problem studied here.

The computational efficiency of Hybrid NS–LB method over LBM and FVM methods to analyze macro-/mesoscale problems has been reported previously by other researchers in references [24,25,35] (in those works, mesoscale refers to continues flow regime with no- slip boundary treatment on solid walls). Moreover, there are many investigations in the literature comparing the computational efficiency of LBM over NS-based numerical methods in porous media and NS-based numerical methods over LBM for the study of macroscopic flow behavior. For instance, Bernsdorf et al. [33] compared lattice gas automata (LGA) and FVM for simulation

Table 2 Effects of time step size on the pure FVM computation time with respect to the pure LBM at $Re = 200$

Numerical method	Time step size	Number of sub-iteration per time step	Total CPU time
Pure FVM	$1 \times \Delta t_{LBM}$	2	$8.48 \times$ LBM CPU Time
	$10 \times \Delta t_{LBM}$	5	$2.32 \times$ LBM CPU Time
	$50 \times \Delta t_{LBM}$	10	$0.84 \times$ LBM CPU Time
	$100 \times \Delta t_{LBM}$	10	$0.44 \times$ LBM CPU Time
	$200 \times \Delta t_{LBM}$	15	$0.33 \times$ LBM CPU Time

of flow in complex geometries (e.g. porous media). They indicated that LGA is computationally more efficient for simulating flow inside porous media. Yoshino et al. [34] conducted a similar comparison between LBM and FDM for flow through a porous structure and came up with the same conclusion. Therefore, LBM is particularly suitable for pore-scale simulation, because of its capability of handling flow around complex geometries [35]. Conversely, for general macroscale problems, it has been indicated in the literature that the computational efficiency of LBM is much lower than conventional CFD methods [36,37].

As stated before, in the present section, the computational efficiency of the hybrid method is compared with both pure LBM and pure FVM. To achieve this task, flow around squared cross-sectional cylinder (one of the main test cases of the present work) is simulated, using pure LBM, pure FVM, and hybrid FVM–LBM methods. The same computational grid (uniform squared grid) was used in all cases. In hybrid FVM–LBM case, 1/3 of the computational grid was specified for LBM and the rest was used for FVM. The flow Reynolds number, based on cylinder height and maximum inlet velocity, was 200 and the physical domain was selected in such a way that the required RAM (computer Random Access Memory) did not exceed 4 GB (maximum RAM of in used computer) in all test cases (LBM, FVM, and hybrid FVM–LBM). It is worthy to note that the pure FVM and pure LBM required the highest and the lowest computer RAM (on the same computational grid), respectively. Since all test cases were unsteady, the computational time corresponding to one period of CL variation was measured and compared for pure LBM, FVM, and hybrid FVM–LBM.

Table 2, presents the ratio of pure FVM computational time to pure LBM one for various FVM time step sizes. These results are measured by solving the problem discussed in previous paragraph using pure FVM and LBM. Additionally, the number of sub-iterations per time step for FVM is shown in this table. In contrast to pure LBM, the time step size of FVM is not limited according to stability considerations (because of its semi-implicit nature) and can be chosen freely with respect to the problem physical timescales. In this work, the minimum macroscale vortex shedding timescale (which occurs for porously covered cylinder at $Re = 240$ and porosity of 0.94) is 45250 Δt_{LBM}, which allows us to safely use the time step size of 400 Δt_{LBM} for FVM in both pure FVM and hybrid FVM–LBM. However, in subsequent simulations (reported in result discussion section), the FVM time step size in hybrid FVM-LBM is 100 Δt_{LBM}. Recall, flow in the mesoscale (LBM) portion of the computational domain is still in continuous regime, but its time and length increments are much smaller than that of the macroscale (FVM) part (based on the oscillations of the lift coefficient).

Because of semi-implicit nature of FVM, as illustrated in Table 2, the computational time of pure FVM is reduced by increasing FVM time step due to less required time steps in each period of CL variations. For instance, when the time step of FVM is set equal to LBM, the computational time of FVM is nearly 8.5 times that of LBM. This result is logical, because the number of computations performed per each time step in LBM is much lower than that of semi-implicit FVM. However, as indicated in Table 2, for higher time steps, the total CPU time of FVM decreases monotonically (compared to LBM). Eventually, as illustrated in Table 2, for $\Delta t > 50 \times \Delta T_{LBM}$, the computational time of FVM becomes lower than that of LBM.

Therefore, from computational cost viewpoint, the choice of a suitable numerical approach strongly depends on physical timescales of the problem. For example, when the physical timescale of a problem is in the order of LBM time step size (such as pore-scale simulation of flow inside of porous media), it is clear that LBM is the most suitable choice. On the other hand, when the physical timescales of a problem are so large that allows us to use very large time steps (such as vortex shedding from bluff bodies), the NS- based FVM is more efficient than LBM. Thus, in a multi-scale problem, where both macro- and mesoscales of the physical events are important (such as interaction of flow with porously covered squared cylinder or fully porous cylinder), using hybrid methods is the best choice.

As stated before, in a multi-scale problem (like the one in this paper), there are at least two physical timescales which need considerably different time steps for simulation. So, for each time step of the macro-level solver, several time steps of the meso-level solver are needed for synchronization purpose. Here, for the hybrid FVM–LBM, 100 iterations of LBM are needed during each FVM time step. Now, if a single FVM

Table 3 Comparison the computation time of pure FVM and hybrid methods in a meso–macroscale problem to find the most efficient method

Numerical method	Time step size	Number of Sub-iteration per time step	Total CPU time
Pure FVM	$1 \times \Delta t_{\text{LBM}}$	2	$8.48 \times$ LBM CPU Time
	$10 \times \Delta t_{\text{LBM}}$	5	$4.37 \times$ LBM CPU Time
	$50 \times \Delta t_{\text{LBM}}$	10	$3.39 \times$ LBM CPU Time
	$100 \times \Delta t_{\text{LBM}}$	10	$3.12 \times$ LBM CPU Time
	$200 \times \Delta t_{\text{LBM}}$	15	$3.05 \times$ LBM CPU Time
Hybrid FVM–LBM	$1 \times \Delta t_{\text{LBM}}$	2	$6.14 \times$ LBM CPU Time
	$10 \times \Delta t_{\text{LBM}}$	5	$1.78 \times$ LBM CPU Time
	$50 \times \Delta t_{\text{LBM}}$	10	$0.92 \times$ LBM CPU Time
	$100 \times \Delta t_{\text{LBM}}$	10	$0.62 \times$ LBM CPU Time
	$200 \times \Delta t_{\text{LBM}}$	15	$0.55 \times$ LBM CPU Time

is used instead of hybrid FVM–LBM to solve such a multi-scale problem, the mesoscale part of the domain (porous region) still must be solved with LBM time step to resolve correct physics. While as indicated in Table 2, the efficiency of a single macroscale solver such as FVM in mesoscale time step size like Δt_{LBM} is much lower than those of pure LBM. Thus, the pure FVM is very efficient only in the macroscale portion of the computational domain, whereas in the mesoscale part, LBM is much better.

Accordingly, the overall computational time in a multi-scale simulation is the sum of the computational times of different scales subregions. For instance, in the present article, 1/3 of the computational domain was solved with Δt_{LBM} and the rest with time step size of $100 \times \Delta t_{\text{LBM}}$; based on Table 2 information, the total computational cost of pure FVM and hybrid FVM–LB methods can be calculated as follows:

Method	Time
Fot pure LBM:	Total CPU Time = LBM CPU Time
Fot pure FVM:	Total CPU Time $= \frac{1}{3} \times [8.48 \times$ LBM CPU Time$] + \frac{2}{3} \times [0.44 \times$ LBM CPU Time$] = 3.12 \times$ LBM CPU Time
Fot hybrid FVM–LBM:	Total CPU Time $= \frac{1}{3} \times [$LBM CPU Time$] + \frac{2}{3} \times [0.44 \times$ LBM CPU Time$] = 0.627 \times$ LBM CPU Time

Based on these results, the computational time of pure FVM was five times that of the hybrid FVM–LB method. This proves the computational efficiency of hybrid FVM–LB method over pure FVM. On the other hand, if the entire of the computational domain is analyzed using a single LBM solver (in the same grid resolution as hybrid FVM–LB method), the computational cost is 1.6 times of hybrid FVM–LBM (due to its considerably smaller time step size; $\Delta T_{\text{FVM}}/100$). The same computations were performed for some other macroscale time steps, and the related results were summarized in Table 3. It should be noted here that although the data in Table 3 computed using above-mentioned relations, the actual CPU time of hybrid FVM–LB and pure FVM solvers match well (less than 2 percent error) with them. This shows the validity of information listed in Table 3. According to Table 3, it is apparent that the computational efficiency of hybrid LBM–FVM is much higher than those of pure FVM in simulating the meso–macroscale problems, like that investigated here. Thus, the hybrid FVM–LBM not only increases the simulation accuracy with respect to the pure FVM (due to the pore-scale modeling) but also improves the computational efficiency comparing to both pure FVM and LBM.

6 Results and discussion

Numerical simulations have been performed to examine the influence of porosity and Reynolds number for flow around a porous, a solid, and a porously covered solid squared section cylinder located at the middle of a channel. As stated before, in this study, the flow inside porous media is analyzed in pore scale using LBM. All porous structures examined here are constructed from several squared section cylinders that are arranged in staggered form. In this section, detailed comparisons of instantaneous velocity and aerodynamic quantities, such as mean drag coefficient, lift coefficient amplitude, and Strouhal number, are presented.
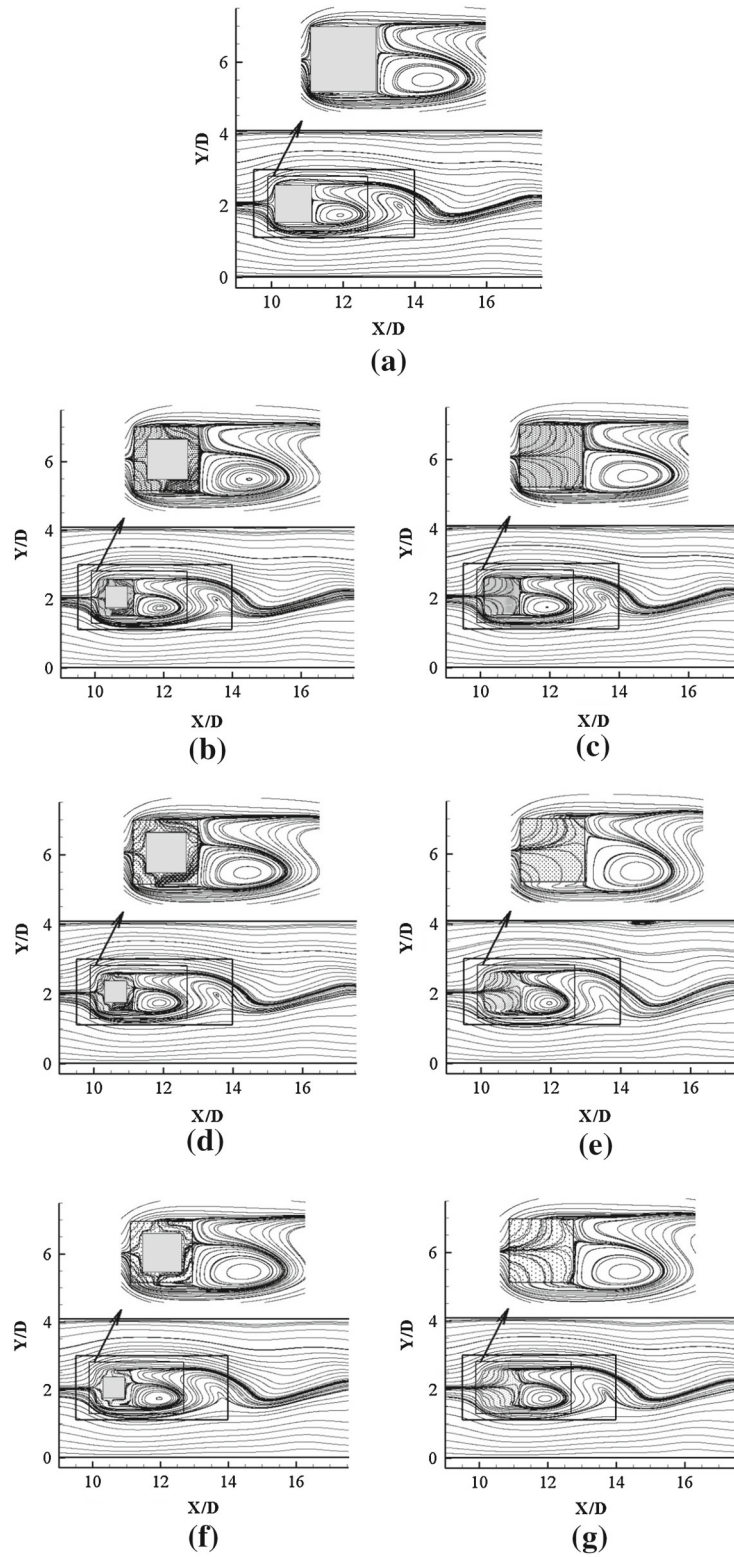
Fig. 6 Streamline contours at $Re = 120$ for different obstacle shapes and for $\varepsilon = 0.75$, 0.85, and 0.94. **a** solid block, **b** porous cover $\varepsilon = 0.75$, **c** porous block $\varepsilon = 0.75$, **d** porous cover $\varepsilon = 0.85$, **e** porous block $\varepsilon = 0.85$, **f** porous cover $\varepsilon = 0.94$, **g** porous block $\varepsilon = 0.94$
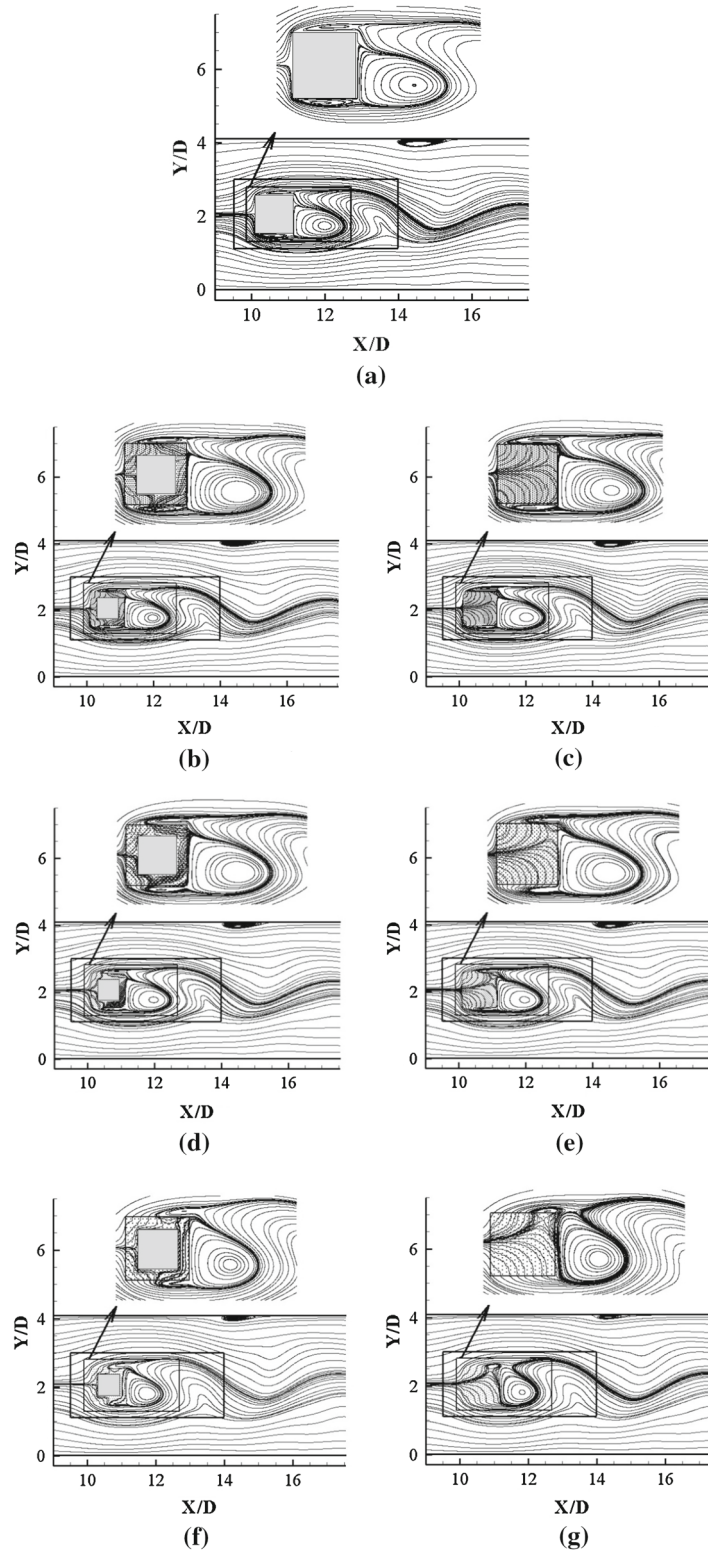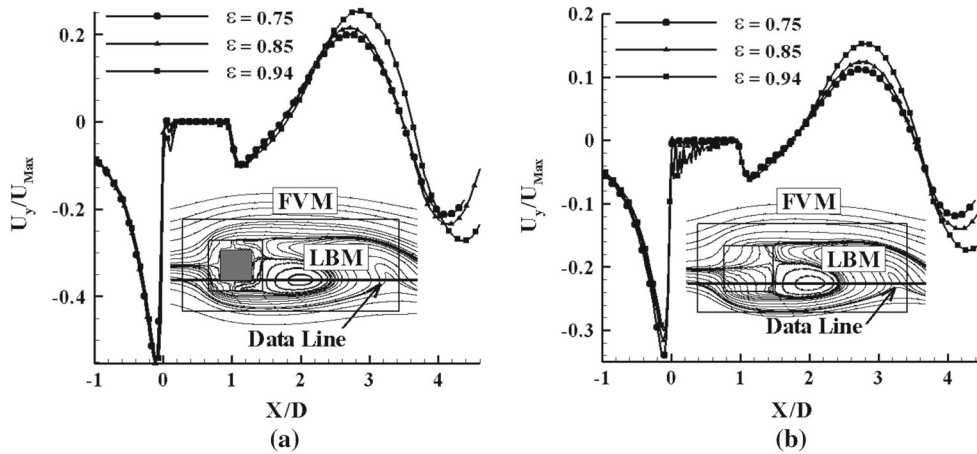
Fig. 7 Streamline contours at $Re = 200$ for different obstacle shapes and for $\varepsilon = 0.75$, 0.85, and 0.94. **a** solid block, **b** porous cover $\varepsilon = 0.75$, **c** porous block $\varepsilon = 0.75$, **d** porous cover $\varepsilon = 0.85$, **e** porous block $\varepsilon = 0.85$, **f** porous cover $\varepsilon = 0.94$, **g** porous block $\varepsilon = 0.94$

Fig. 8 Lateral velocity component profiles for different porosities at $Re = 120$. **a** Porously covered solid cylinder, **b** porous cylinder

Figure 6 shows the wake flow pattern at $Re = 120$ for different porosities, i.e., $\varepsilon = 0.75, 0.85$, and 0.94, when lift coefficient reaches its maximum. Similarly, in Fig. 7, these vortex patterns are demonstrated for $Re = 200$ ($Re = u_{max} D/\upsilon$). Based on this figures, the following results were obtained.

First, the streamlines crossing the interface of LBM and FVM (the outer rectangular solid line) are smooth, showing suitable accuracy of information exchanged between these two flow solvers in both time and space. For $Re = 120$, as illustrated in Fig. 6, the mean flow momentum is relatively low and the portion of the fluid passing through porous obstacles is not considerable. Additionally, this flow does not have enough momentum to move fast through the porous obstacle and could not influence the main vortex structure. Consequently, as shown in Fig. 6, the position and the size of the wake flow vortices are nearly similar for all obstacle shapes and porosity. Nevertheless, the size of the main vortex is slightly increased for both porous block and porously covered squared cylinder (Fig. 6b, d, e, f, g) as the porosity increases. In order to clarify this change in the main vortex size and strength for the proposed porous geometries, non-dimensioned lateral velocity component (u_y/u_{max}; u_{max} is the maximum inlet velocity) is plotted along the illustrated longitudinal line at $Re = 120$ in Fig. 8. As shown in this figure, the pick to pick distances along both x and y axes are increased by increasing porosity (for both porous covering squared and porous block). Hence, it can be concluded that the strength and the size of the main vortex is larger for higher porosity.

As shown in Fig. 7b, c for ($Re = 200$ at $\varepsilon = 0.75$), the flow patterns for both porously covered solid cylinder and porous cylinder are quite identical to those of the non-porous one. As discussed before, the permeability of porous material at $\varepsilon = 0.75$ is too low to permit fluid to flow freely through the porous block which affect the wake flow pattern considerably, but as porosity increases, the permeability of porous media will increase too and thereby it permits more fluid to pass through the porous media and changes the vortex pattern in the wake flow. As an illustration, increasing porosity (Fig. 7d–g) decreases the longitudinal length (*x* direction size) of the main trailing edge vortex and increases its lateral (y-direction) size. Eventually, at $\varepsilon = 0.94$ (Fig. 7f, g), the trailing edge vortex covers the whole length of the rear side (downstream edge) of the blocks.

Figure 7 demonstrates that for $Re = 200$, increasing porosity, the size of upper and lower vortices decreases and their positions move more downstream for both porous and porously covered solid cylinders. However, this phenomenon is more obvious for the case of porous cylinder than for porously covered one. This is due to the easier flow motion inside the porous media (from front face of the block toward its upper and lower sides) at larger permeability. Thus, the amount of the fluid injected to the surrounding (from upper and lower sides of porous block) increases at higher porosity. Based on this figure, as more fluid is injected, the size of the side vortices decreases and they move further downstream.

For the porously covered solid cylinder (as shown in Figs. 6, 7), a portion of trailing edge vortices penetrate into the porous layer and touches the trailing edge of the central solid block. This unique behavior is the result of a relatively low- pressure region existing just behind the central solid cylinder (middle part of the porously covered cylinder). Moreover, as depicted in Figs. 6 and 7, the side vortices are mixed with wake vortices through the porous layer in porously covered cylinder case. As porosity increases, this phenomenon becomes more pronounced for porously covered cylinder. Thus, the shape and the size of the porously covered cylinder are noticeably different from those of fully porous and solid cylinders.
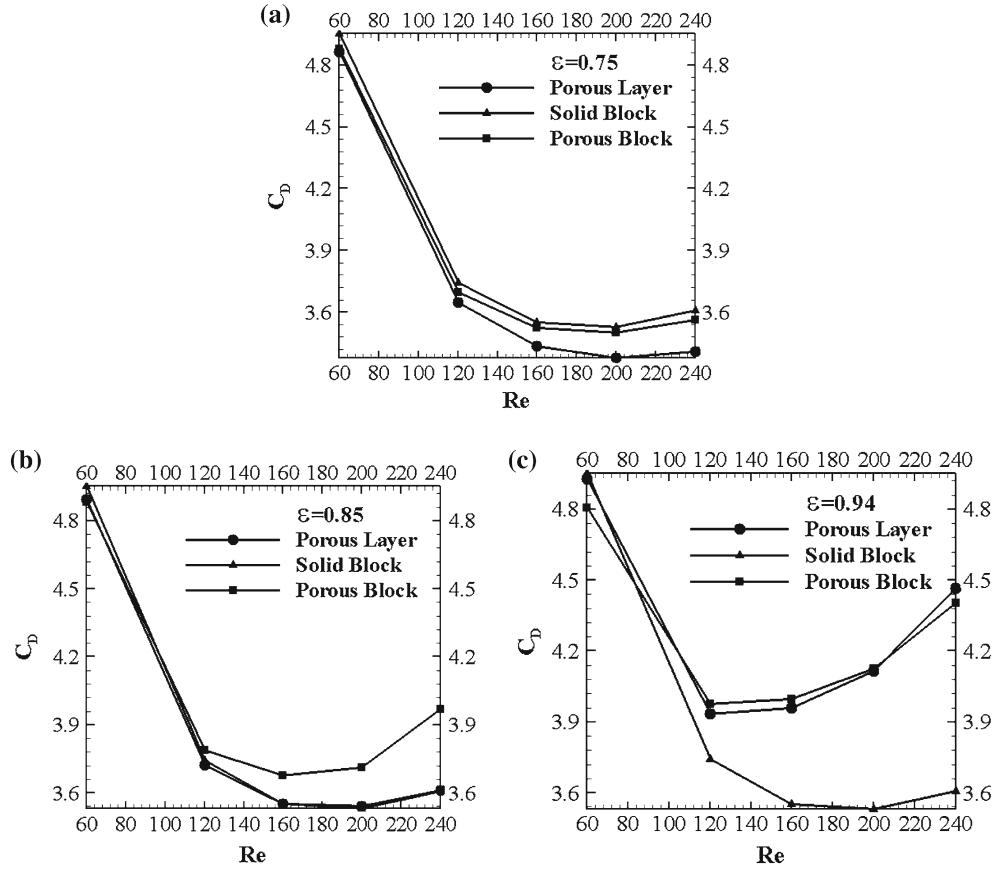
Fig. 9 The effect of different obstacle shapes and porosities on variation of mean drag coefficient with Re

Note, Reynolds numbers of 60, 120, 160, 200, and 240 were studied here; however, only the flow patterns related to $Re = 120$ and 200 are shown in Figs. 7 and 8. From these figures, it is clear that the lateral (y-direction) width of the recirculation region is larger at $Re = 200$ (compared to $Re = 120$), while the longitudinal (x-direction) length of this region is larger for $Re = 120$, specially at $\varepsilon = 0.85$ and $\varepsilon = 0.94$. Furthermore, the size of side vortices (upper and lower sides of the block) for $Re = 200$ is larger than those observed for $Re = 120$. As expected, the size and the strength of all vortex structures increase for larger Reynolds numbers.

To investigate the hydrodynamic characteristics of obstacle shapes in more details, mean drag coefficient, amplitude of lift coefficient, and Strouhal number were computed at various porosities and Reynolds numbers. Lift and drag coefficients are defined as:

$$C_D = \frac{F_D}{\rho u_{\max}^2 D} \quad C_L = \frac{F_L}{\rho u_{\max}^2 D} \tag{15}$$

where $u_{\max}$ and D are maximum inlet velocity and obstacle height, respectively. The momentum-exchange method of Mei et al. [38] was employed to compute lift (F_L) and drag (F_D) forces as follows:

$$F = \sum_{\text{all } xb} \sum_{\alpha \neq 0}^{N_d} e_\alpha \left[\tilde{f}_\alpha (x_b, t) + \tilde{f}_{\tilde{\alpha}} (x_b + e_{\tilde{\alpha}} \delta t, t) \right] (1 - w (x_b + e_{\tilde{\alpha}} \delta t)), \tag{16}$$

in which x_b is a solid boundary lattice and $\tilde{f}_{\tilde{\alpha}}$ is post-collision distribution function. $w (i, j)$ is a scalar array that is set to 1 for solid nodes and 0 for those lattice nodes occupied by fluid. For a given nonzero velocity, e_α and $e_{\tilde{\alpha}}$ represent the velocity in opposite direction, i.e., $e_\alpha \equiv -e_{\tilde{\alpha}}$ [38].

Figure 9 shows the time-averaged drag coefficient versus Reynolds number for different obstacle shapes and porosities. As shown in Fig. 9a, at $\varepsilon = 0.75$, the porously covered cylinder and the solid cylinder have the
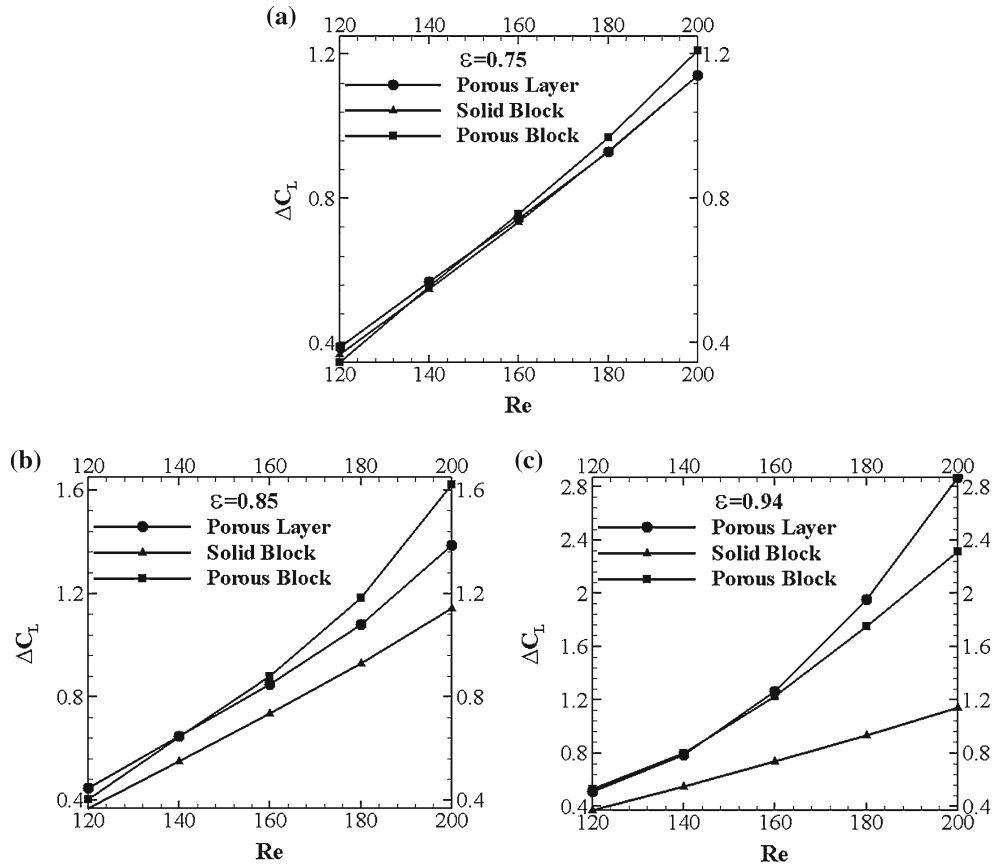
Fig. 10 The effect of different obstacle shapes and porosities on variation of lift coefficient amplitude versus *Re*

lowest and highest drag coefficients (for the entire range of *Re* numbers), respectively. However, as porosity increases (Fig. 9b, c), the drag coefficient of porous obstacles (both porous covering and fully porous block cylinders) increases. As a result, the drag coefficient of porous obstacles at $\varepsilon = 0.94$ (Fig. 9c) is much higher than that of solid cylinder. Additionally, for the case of porously covered cylinder, although just a portion (nearly half) of the cylinder is filled with porous material, its drag coefficient is quite close to fully porous cylinder for all examined porosities and Reynolds numbers.

Note, the value of momentum loss resulting from the presence of porous media is well correlated with the amount of fluid flow through the porous blocks. For instance, at $\varepsilon = 0.75$, due to higher flow resistance, an insignificant part of the main flow goes through the porous media and the major part bypasses. Accordingly, there is not a considerable drag deficit, despite the fact that the existence of porous media has contributed to the reduction of skin friction drag and hence small reduction of the total drag coefficient (Fig. 9a). For higher porosity, due to higher void volume inside the porous cylinders (Fig. 9b, c), the portion of fluid which passes through porous media increases. Consequently, it is obvious that a higher momentum is absorbed by porous media, and hence, higher drag force is produced. Finally, it is worthy to note that the above discussion is true as long as the pressure difference between the front and back sides of the proposed porous obstacles (pressure drag) has a minor contribution in total drag force (compared to viscous momentum losses occurring through the porous media). Thus, it is expected that as the Reynolds number increases, the pressure drag becomes dominant and the total drag coefficient for porous geometries decreases with respect to the solid squared cylinder.

The amplitude of lift coefficient for various obstacle shapes at different Reynolds numbers ($Re = 120$–200) and porosities ($\varepsilon = 0.75$, 0.85, and 0.94) is shown in Fig. 10. As shown in this figure, for all obstacle shapes and porosities, the amplitude of lift coefficient increases monotonically, as *Re* increases. This is because, the effects of vortex structures, caused by increasing mean flow Reynolds number, becomes more dominant.

At $\varepsilon = 0.75$, as demonstrated in Fig. 10a, the discrepancies among different cases is negligible. This confirms that the resulting vortex structure for different obstacles used is fairly similar at this ε. Nevertheless, for higher porosities ($\varepsilon = 0.85$ and 0.94), as shown in Fig. 10b, c, the discrepancies increases. According to
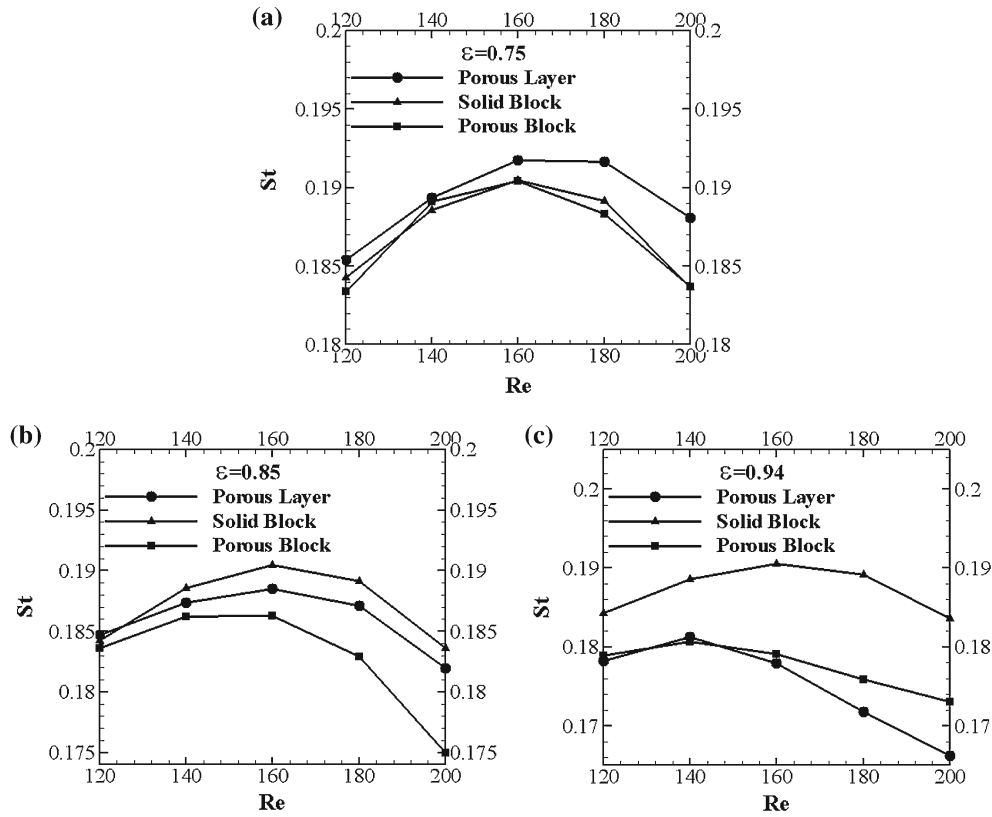
Fig. 11 Effect of different obstacle shapes and porosities on variation of Strouhal number with *Re*

these figures, the differences become more, as Reynolds number and porosity increase. Furthermore, among obstacle shapes employed, it is evident that at $\varepsilon = 0.85$, the amplitude of lift coefficient for porous cylinder is larger than those of porously covered and solid cylinders, while at $\varepsilon = 0.94$,, the porously covered solid cylinder has the highest value. As stated before, increasing Reynolds number and porosity are the main reasons for having easier fluid flow through porous media, causing alteration in the flow structures (this creates more variation in lift coefficient).

Another important quantity taken into consideration here is Strouhal number (St), i.e.,

$$St = \frac{fD}{u_{max}}, \tag{17}$$

where f is the lift force frequency. Note, the frequency of lift coefficient is twice that of the drag coefficient, which is consistent with the results reported by Chen et al. [7]. The variation of the Strouhal number versus *Re* at different obstacle shapes and porosities is shown in Fig. 11. From this figure, for all porosities, at lower Reynolds numbers, Strouhal number increases with *Re* and then decreases after reaching a maximum value. Also, for porously covered and fully porous cylinders, the Reynolds number corresponding to maximum Strouhal number decreases, as porosity increases. This behavior is more evident for porously covered solid cylinder. In addition, for a given porous obstacle (fully porous or porously covered cylinders), Strouhal number and hence the frequency of vortex shedding reduces by increasing porosity. It is also noteworthy that the higher Reynolds number corresponds to higher reduction in St (Fig. 11). Among the employed obstacle geometries, changes in porosity mostly influence the shedding frequency of porously covered solid cylinder. Since Strouhal number for this geometry is highest at $\varepsilon = 0.75$ (for entire range of *Re* numbers), it becomes the lowest as ε increases. Overall, the Strouhal number (such as lift and drag coefficients) is strongly affected by changes in porosity for the porous obstacles studied here.

To investigate flow evolution in more details, Fig. 12 shows lift and drag coefficients versus the non-dimensioned time t/τ (where τ is the period of lift coefficient oscillations) for various obstacle shapes and porosities (at $Re = 240$). Note, at the Reynolds number chosen here, the difference between flow characteristics
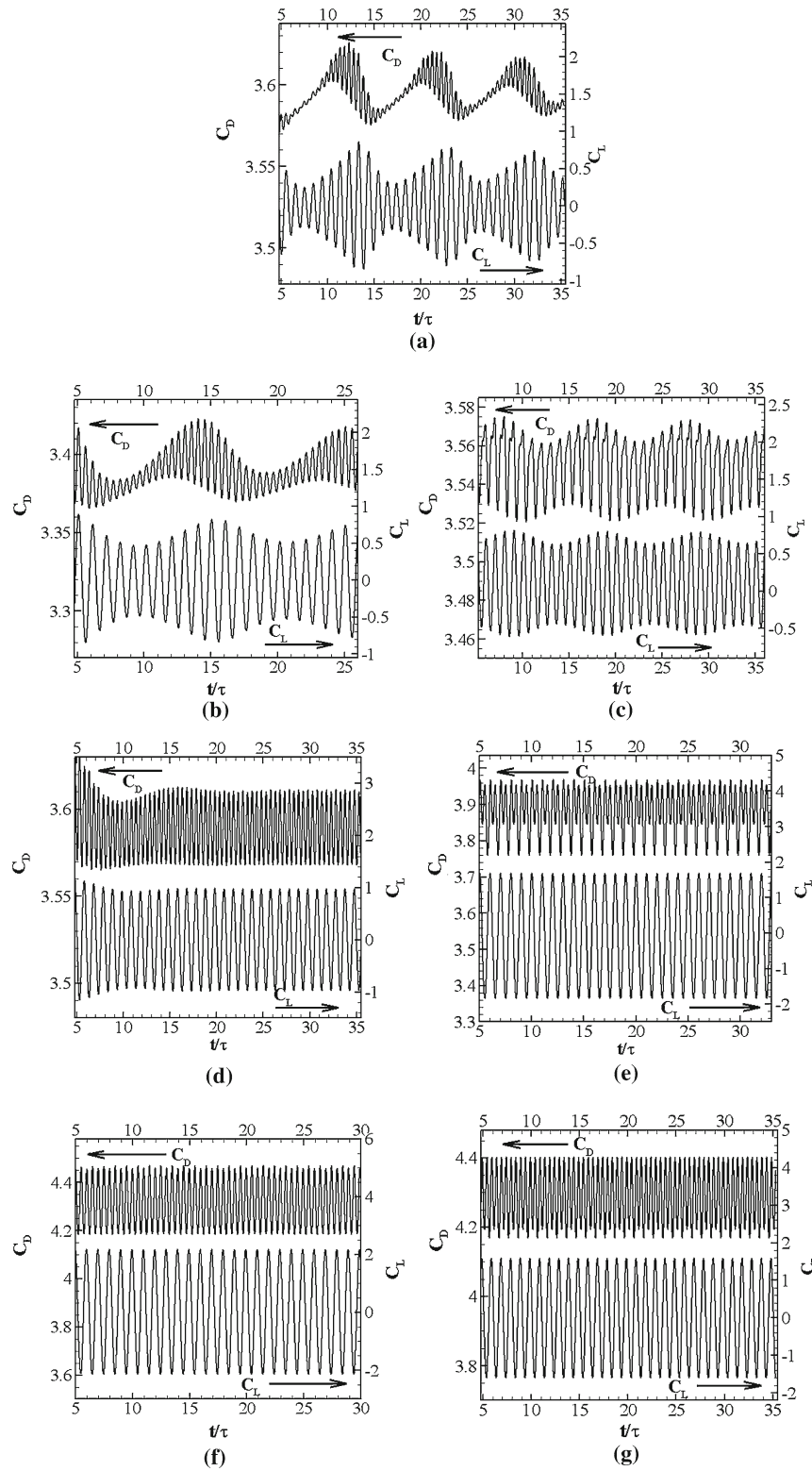
Fig. 12 Time history of lift and drag coefficients for different obstacle shapes and porosities at $Re = 240$. **a** Solid cylinder, **b** porously covered cylinder at $\varepsilon = 0.75$, **c** porous cylinder at $\varepsilon = 0.75$, **d** porously covered cylinder at $\varepsilon = 0.85$, **e** porous cylinder at $\varepsilon = 0.85$, **f** porously covered cylinder at $\varepsilon = 0.94$, **g** porous cylinder at $\varepsilon = 0.94$

Table 4 Change in Strouhal number variation and lift and drag coefficients and amplitudes for various obstacle geometries at $\varepsilon = 0.75$ and $Re = 240$

Obstacle geometry	ΔSt	ΔA_{CL}	ΔA_{CD}
Solid cylinder	0.0138	0.941	0.0319
Porously covered solid cylinder	0.0081	0.697	0.0293
Porous cylinder	0.0054	0.320	0.0168

of employed geometries is more distinct. As illustrated in Fig. 12a, for the solid cylinder case, the amplitude of temporal variation in C_L and C_D is not constant (it changes periodically). This is more obvious for drag coefficient and is not observed at lower Reynolds numbers examined here ($Re \leq 200$). Likewise, for porously covered and for fully porous cylinders, at $\varepsilon = 0.75$ (Fig. 12b, c), the amplitude of lift and drag coefficients change with time, regardless of the fact that this variation in amplitude reduces for these two cases (compared to solid cylinder case).

It is worth noting that the frequency of temporal variation of C_L and C_D changes in the same way. The range of variations in Strouhal number (ΔSt) and in the amplitude of lift and drag coefficients (ΔA_{CL} and ΔA_{CD}) for different obstacle shapes at $\varepsilon = 0.75$ and $Re = 240$ are listed in Table. 4. The comparison of data shows that the change in lift and drag amplitude and St number for porously covered and fully porous cylinders are much lower than those of solid cylinder. Thus, the porous media acts like a filter and produces more uniform shedding pattern compared to those of solid cylinder.

In order to study the filtering behaviors of porously covered case in more details, higher Reynolds numbers (including $Re = 260$, 280 and 300) were also examined. It is worthy to mention that, at $Re = 300$, the temporal variation of C_L and C_D for squared solid cylinder becomes uniform again (similar to those previously observed for $Re < 240$), while at $Re = 260$ and 280, the shape of C_L and C_D variations with respect to time for all obstacle shapes is quite similar to those of $Re = 240$ (illustrated in Fig. 12). Thus, in the range of $240 < Re < 300$, the frequency and the amplitude of C_L and C_D for squared solid cylinder changes with time. The porous covering acts like a filter and produce quite uniform C_L and C_D oscillations profiles for $\varepsilon \geq 0.85$.

For $\varepsilon = 0.85$ and 0.94, as shown in Fig. 12e, g, drag coefficient oscillation for fully porous cylinder has twin pick pattern, while the porously covered solid cylinder has single pick pattern. On the other hand, the lift coefficient oscillation has a single pick pattern for both porously covered and fully porous cylinders at $\varepsilon = 0.85$ and 0.94 (Fig. 12d–g), which is consistent with the results obtained by Jue [6].

Furthermore, as illustrated in Fig. 12, the fluctuating amplitude of both lift and drag coefficients enlarges for higher porosities, while changes in drag coefficient is not as significant as that of lift coefficient. As depicted in Fig. 12, this behavior is common for both fully porous and porously covered cylinders. The similar trends for lift and drag coefficients is also reported by Jue [6] for fully porous cylinder.

7 Conclusion

A numerical study of a two-dimensional unsteady laminar flow over a squared section cylinder located at the middle of a plain channel has been performed here. Three different cases of fully solid, fully porous, and porously covered solid cylinders were examined with a hybrid NS (FVM)–LBM (MRT) flow solver. All cases were studied with different porosities (permeability or Darcy number) and Reynolds numbers. In order to increase the computational precision, all porous cases were treated in pore level. The main conclusions of this work are listed bellow:

1. The proposed FV-LB (MRT) method possesses relatively high accuracy to simulate an unsteady separated flow behind porous structures, and its computational cost is considerably lower than fully LBM and FVM simulations. This is due to multi-scale nature of such problems, which is well matched with the logic of hybrid FV-LB method. Additionally, the employed LB-MRT method simulates flow inside porous media fairly well (compared to NS computations).

2. The size and shape of the sides and wake vortex structures of porously covered and fully porous cylinders are quite identical to those of the solid squared cylinder case at $\varepsilon = 0.75$ (for the entire range of Reynolds numbers examined). However, in higher porosities, i.e. $\varepsilon = 0.85$ and $\varepsilon = 0.94$, since more fluid can pass through the porous media, the sides and the wake flow vortex patterns are different for porously covered and fully porous cylinders (especially in higher Reynolds numbers; $Re = 200$).

3. For the porously covered cylinder, the wake flow vortices penetrate into the porous layer from the rear side (downstream) and touch the central solid cylinder (for all porosities and Reynolds numbers examined). Thus, the size and shape of wake vortices for porously covered cylinder is different from those are observed in fully porous and solid cylinders.
4. The drag coefficients of porously covered and fully porous cylinders are quite close (for the entire range of Reynolds numbers examined) and increase noticeably with respect to solid cylinder as porosity increases.
5. Effects of porosity on flow structures and hydrodynamic variables (drag and lift coefficients and Strouhal number) are considerable for both porously covered and fully porous cylinders. These effects are more pronounced for the case of porously covered cylinder.
6. Porous covering acts like a filter for $240 \leq Re \leq 300$ and produces uniform lift and drag coefficient oscillations (uniform vortex shedding). This becomes more clear when porosity increases for both porously covered and fully porous squared section cylinders.

References

1. Williamson, C.H.K., Govardhan, R.: Vortex-induced vibrations. Ann. Rev. Fluid Mech. **36**, 413–455 (2004)
2. Bruneau, C.H., Mortazavi, I.: Passive control of bluff body flow using porous media. Int. J. Numer. Methods Fluids **46**, 415–433 (2004)
3. Bhattacharyya, S., Singh, A.K.: Augmentation of heat transfer from a solid cylinder wrapped with a porous layer. Int. J. Heat Mass Transf. **52**, 1991–2001 (2009)
4. Perng, S.W., Wu, H.W., Jue, T.C.: Numerical investigation of heat transfer enhancement on a porous vortex generator applied to a block-heated channel. Int. J. Heat Mass Transf. **55**, 3121–3137 (2012)
5. Huang, P.C., Vafai, K.: Passive alteration and control of convective heat transfer utilizing alternate porous cavity-block wafers. Int. J. Heat Fluid Flow **15**, 48–61 (1994)
6. Jue, T.C.: Numerical analysis of vortex shedding behind a porous square cylinder. Int. J. Numer. Methods Heat Fluid Flow **14**, 649–663 (2004)
7. Chen, X., Yu, P., Winoto, S.H.: Numerical analysis for the flow past a porous square cylinder based on the stress-jump interfacial-conditions. Int. J. Numer. Methods Heat Fluid Flow **18**, 635–655 (2008)
8. Bruneau, C.H., Mortazavi, I.: Numerical modelling and passive flow control using porous media. Comput. Fluids **37**, 488–498 (2008)
9. Rong, F.M., Guo, Z.L., Lu, J.H., Shi, B.C.: Numerical simulation of the flow around a porous covering square cylinder in a channel via lattice Boltzmann method. Int. J. Numer. Methods Fluids **65**, 1217–1230 (2011)
10. Wu, H.W., Wang, W.B.: Unsteady convective heat transfer over a heated square porous cylinder in a channel. Int. J. Heat Mass Transf. **53**, 1927–1937 (2010)
11. Perng, S.W., Wu, H.W., Wang, R.H., Jue, T.C.: Unsteady convection heat transfer for a porous square cylinder varying cylinder-to-channel height ratio. Int. J. Therm. Sci. **50**, 2006–2015 (2011)
12. Liang, Y.Y., Chuan, H.P., Fu, Y.C., Jen, C.Y.: Numerical study of heat transfer of a porous-block-mounted heat source subjected to pulsating channel flow. Numer. Heat Transf. Part A Appl. **54**, 426–449 (2008)
13. Cancelliere, A., Chang, C., Foti, E., Rothman, D.H., Succi, S.: The permeability of a random medium: comparison of simulation with theory. Phys. Fluids A **2**, 2085–2088 (1990)
14. Inamuro, T., Yoshino, M., Ogino, F.: Lattice Boltzmann simulation of flows in a three-dimensional porous structure. Int. J. Numer. Methods Fluids **29**, 737–748 (1999)
15. Yoshino, M., Inamuro, T.: Lattice Boltzmann simulations for flow and heat/mass transfer problems in a three-dimensional porous structure. Int. J. Numer. Meth. Fluids **43**, 183–198 (2003)
16. Wang, M., He, J., Yu, J., Pan, N.: Lattice Boltzmann modeling of the effective thermal conductivity for fibrous materials. Int. J. Therm. Sci. **46**, 848–855 (2007)
17. Verma, N., Mewes, D.: Lattice Boltzmann methods for simulation of micro and macro transport in a packed bed of porous adsorbents under non-isothermal condition. Comput. Math. Appl. **58**, 1003–1014 (2009)
18. Javaran, E.J, Gandjalikhan Nassab, S.A., Jafari, S.: Thermal analysis of a 2-D heat recovery system using porous media including lattice Boltzmann simulation of fluid flow. Int. J. Therm. Sci. **49**, 1031–1041 (2010)
19. Li, Q., Zhao, K., Xuan, Y.M.: Simulation of flow and heat transfer with evaporation in a porous wick of a CPL evaporator on pore scale by lattice Boltzmann method. Int. J. Heat Mass Transf. **54**, 2890–2901 (2011)
20. Albuquerque, P., Alemansi, D., Chopard, B., Leone, P.: Coupling a Lattice Boltzmann and Finite Difference Scheme. International Conference on Computational Science. Krakow, Poland (2004)
21. Christensen, A., Graham, S.: Multiscale lattice Boltzmann modeling of phonon transport in crystalline semiconductor material. Numer. Heat Transf. B **57**, 89–109 (2010)
22. Joshi, H., Agarwal, A., Puranik, B., Shu, C., Agrawal, A.: A hybrid FVM–LBM method for single and multi-fluid compressible flow problems. Int. J. Numer. Methods Fluids **62**, 403–427 (2010)
23. Luan, H.B., Xu, H., Chen, L., Sun, D.L., Tao, W.Q.: Numerical illustrations of the coupling between lattice Boltzmann method and finite-type macro-numerical methods. Numer. Heat Transf. B **57**, 147–171 (2010)
24. Luan, H.B., Xu, H., Chen, L., Feng, Y.L., He, Y.L., Tao, W.Q.: Coupling of finite volume method and thermal lattice boltzmann method and its application to natural convection. Int. J. Numer. Meth. Fluids **70**, 200–221 (2012)
25. Chen, L., Luan, H.B., Feng, Y.L., Song, C., He, Y.L., Tao, W.Q.: Coupling between finite volume method and lattice Boltzmann method and its application to fluid flow and mass transport in proton exchange membrane fuel cell. Int. J. Heat Mass Transf. **55**, 3834–3848 (2012)

26. Boomsma, B., Poulikakos, D., Zwick, F.: Metal foams as compact high performance heat exchangers. Mech. Mater. **35**, 1161–1176 (2003)
27. Tadrist, L., Miscevic, M., Rahli, O., Topin, F.: About the use of fibrous materials in compact heat exchangers. Exp. Therm. Fluid Sci. **28**, 193–199 (2004)
28. He, X., Zou, Q., Luo, L.S., Dembo, M.: Analytic solution and analysis on non-slip boundary condition for the lattice Boltzmann BGK model. J. Stat. Phys. **87**, 115–136 (1997)
29. Pan, C., Luo, L.S., Miller, C.T.: An evaluation of lattice Boltzmann schemes for porous medium flow simulation. Comput. Fluids **35**, 898–909 (2006)
30. Peng, Y., Shu, C., Chew, Y.T., Niu, X.D., Lu, X.Y.: Application of multi-block approach in the immersed boundary-lattice Boltzmann method for viscous fluid flows. J. Comput. Phys. **218**, 460–478 (2006)
31. Xu, H., Luan, H.B., He, Y.L., Tao, W.Q.: A lifting relation from macroscopic variables to mesoscopic variables in lattice Boltzmann method: derivation numerical assessments and coupling computations validation. Comput. Fluids J. **54**, 92–105 (2012)
32. Breuer, M., Bernsdorf, J., Zeiser, T., Durst, F.: Accurate computations of the laminar flow past a square cylinder based on two different methods: lattice-Boltzmann and finite-volume. Int. J. Heat Fluid Flow **21**, 186–196 (2000)
33. Bernsdorf, J., Durst, F., Schafer, M.: Comparison of cellular automata and finite volume techniques for simulation of incompressible flows in complex geometries. Int. J. Numer. Method Fluids **29**, 251–264 (1999)
34. Yoshino, M., Matsuda, Y., Shao, C.: Comparison of accuracy and efficiency between the lattice Boltzmann method and the finite difference method in viscous/thermal fluid flows. Int. J. Comput. Fluid D **18**, 333–345 (2004)
35. Luan, H.B., Xu, H., Chen, L., Sun, D.L., He, Y.L., Tao, W.Q.: Evaluation of the coupling scheme of FVM and LBM for fluid flows around complex geometries. Int. J. Heat Mass Transf. **54**, 1975–1985 (2011)
36. Pan, C.X., Prins, J.F., Miller, C.T.: A high-performance lattice Boltzmann implementation to model flow in porous media. Comput. Phys. Commun. **158**, 89–105 (2004)
37. Imamura, T., Suzuki, K., Nakamura, T., Yoshida, M.: Acceleration of steady state lattice Boltzmann simulation on non-uniform mesh using local time step method. J. Comput. Phys. **202**, 645–663 (2005)
38. Mei, R., Yu, D., Shyy, W., Luo, L.S.: Force evaluation in the lattice Boltzmann method involving curved geometry. Phys. Rev. E **65**, 1–14 (2002)